## Impact of Spectral Coverage on Parameter recovery in Blazar Modeling

N. Sahakyan, D. Bégué, P. Giommi, 3,4,5 H. Dereli-Bégué, And Asaf Pe'er<sup>2</sup>

 $^1ICRANet\text{-}Armenia,\ Marshall\ Baghramian\ Avenue\ 24a,\ Yerevan\ 0019,\ Armenia$   $^2Department\ of\ Physics,\ Bar\text{-}Ilan\ University,\ Ramat\text{-}Gan\ 52900,\ Israel$ 

<sup>3</sup> Center for Astrophysics and Space Science (CASS), New York University Abu Dhabi, PO Box 129188 Abu Dhabi, United Arab Emirates
<sup>4</sup> Associated to INAF, Osservatorio Astronomico di Brera, via Brera, 28, I-20121 Milano, Italy

<sup>5</sup> Institute for Advanced Study, Technische Universität München, Lichtenbergstrasse 2a, D-85748 Garching bei München, Germany

#### ABSTRACT

Understanding the impact of spectral coverage on parameter recovery is critical for accurate interpretation of blazar spectra. In this study, we examine how the data coverage influences the reliability of parameter estimation within the one-zone synchrotron self-Compton (SSC) framework. Using OJ 287, TXS 0506+056, and Mrk 421 as representative of the low-, intermediate- and high synchrotron peak classes (LSP, ISP and HSP), respectively, we generate synthetic SEDs based on their best-fit models and perform 1,000 fits for each of the 21 observational configurations per source type. Our analysis quantifies the coverage probability for all model parameters, such has the magnetic field strength and the electron luminosity, and reveals that different blazar subclasses exhibit distinct sensitivities to spectral gaps. For LSPs, a minimal dataset comprising optical/UV, X-ray, and GeV  $\gamma$ -ray bands is sufficient for robust parameter inference. In contrast, ISPs and HSPs require broader spectral coverage to constrain the physical parameters. For ISP, we find that reliable parameter recovery can be achieved with two different minimal band combinations: (i) X-ray, high energy  $\gamma$ -ray, and very high energy  $\gamma$ ray data, or (ii) optical/UV, X-ray, and high energy  $\gamma$ -ray data. For HSPs, the minimal configuration enabling reliable parameter recovery includes the optical/UV, X-ray, and very high energy  $\gamma$ -ray bands. We discuss the role of very high energy  $\gamma$ -ray observations, showing that they significantly enhance parameter recovery for HSPs. Our results provide practical guidelines for designing optimized multiwavelength observation campaigns and for assessing the robustness of SSC model inferences under incomplete spectral coverage.

Keywords: Blazars (164) — BL Lacertae objects (158) — Astronomy data modeling (1859) — High Energy astrophysics (739)

#### 1. INTRODUCTION

The study of blazars has entered a new era. The multiplication of multi-wavelength and multi-messenger campaigns is drastically increasing the volume of available data, while the recent advances in both machine learning and modeling enable detailed spectral analysis by fitting state-of-the-art numerical models of blazar emission to observations (Bégué et al. 2024; Sahakyan et al. 2024b; Tzavellas et al. 2024). These developments are expected to lead to a deeper understanding of the physical processes occurring in this kind of active galactic nuclei (AGN).

Email: narek.sahakyan@icranet.org

Blazars are a subclass of AGN characterized by relativistic jets that are closely aligned with our line of sight (Urry & Padovani 1995). Their emission spans the entire electromagnetic spectrum, from radio wavelengths up to high-energy (HE; > 100 MeV) and very high-energy (VHE; > 100 GeV)  $\gamma$ -rays (Padovani et al. 2017). One of the defining properties of blazars is their rapid variability, which can occur on timescales as short as minutes (e.g., Aharonian et al. 2007; Ackermann et al. 2016; Shukla et al. 2018; Aleksić et al. 2014), indicating that their emission is produced in a compact region and that highly energetic processes are taking place in their jets. Blazars are the dominant class of extragalactic sources in the  $\gamma$ -ray sky (Abdollahi et al. 2022), making them key targets for current and upcoming multi-wavelength and multi-messenger observatories.

The multi-wavelength emission of blazars exhibits a characteristic double-peaked structure, with the lowenergy component peaking between the optical and Xray bands, and the HE component extending above the X-ray band. The origin of this emission is still under debate and is typically categorized based on the type of particles responsible for the emission. In leptonic scenarios, where electrons are the primary radiating particles, the low-energy peak is interpreted as synchrotron emission from relativistic electrons, while the HE component is produced from inverse Compton scattering of synchrotron photons produced by the same electron population (synchrotron self-Compton, or SSC, Ghisellini et al. 1985; Maraschi et al. 1992; Bloom & Marscher 1996), or external photons originating from the accretion disk, the broad-line region, or the dusty torus (external Compton, or EC, Dermer et al. 1992; Dermer & Schlickeiser 1994; Sikora et al. 1994; Błażejowski et al. 2000). Instead in hadronic models, the low-energy component is again explained by synchrotron radiation from electrons, but the HE component arises from synchrotron emission by relativistic protons (Mücke & Protheroe 2001) or by secondary particles produced through proton interactions Mannheim & Biermann 1989; Mannheim 1993; Mücke et al. 2003). Recently, the detection of VHE neutrinos spatially coincident with blazars (e.g., IceCube Collaboration et al. 2018a,b; Padovani et al. 2018; Sahakyan et al. 2023) has renewed interest in hadronic and lepto-hadronic models (see, e.g., Böttcher et al. 2013; Ansoldi et al. 2018; Keivani et al. 2018; Murase et al. 2018; Padovani et al. 2018; Sahakyan 2018; Righi et al. 2019; Cerruti et al. 2019; Sahakyan 2019; Gao et al. 2019; Gasparyan et al. 2022), which can naturally account for both the electromagnetic and neutrino emission. However, we only focus on SSC models in this paper.

Blazars are commonly classified based on the peak frequency of their synchrotron component (Padovani & Giommi 1995; Abdo et al. 2010). Sources with an observed synchrotron peak frequency  $\nu_{\rm syn} < 10^{14}$  Hz are categorized as low-synchrotron-peaked (LSP or LBL) blazars. Those with  $10^{14}$  Hz  $< \nu_{\rm syn} < 10^{15}$  Hz are classified as intermediate-synchrotron-peaked (ISP or IBL) blazars, and sources with  $\nu_{\rm syn} > 10^{15}$  Hz are classified as high-synchrotron-peaked (HSP or HBL) blazars. Blazars are also grouped based on the strength of their optical emission lines. Sources with strong, broad emission lines are classified as flat-spectrum radio quasars (FSRQs), while those with weak or absent emission lines are identified as BL Lacertae (BL Lac) objects (Urry & Padovani 1995).

From a theoretical perspective, significant progress has been made in developing numerical models that can satisfactorily describe the physical processes occurring in blazar jets. While these models account for a broad range of relevant mechanisms, their application to large samples of sources or extensive datasets has been limited due to the computational cost associated with scanning the high-dimensional parameter space. Due to the nonlinear dependence of the spectra on the parameters, a fit is essential, as the model parameters and their uncertainties cannot be inferred separately. Recently, the application of neural networks (surrogate models) to the interpretation of observed data especially in the case of blazars, have addressed this limitation by enabling fast and efficient fitting of spectral or temporal emission from relativistic sources (Bégué et al. 2024; Sahakyan et al. 2024b; Tzavellas et al. 2024). This method allows for thousands of fits to be performed in a reasonable time, whereas previously only a few—if any—model realizations could be explored. This is different from the traditional methods relying on presenting a single model that "visually" matches the observations, without performing any statistical inference (see however Finke et al. 2008; Rodrigues et al. 2024; Sciaccaluga et al. 2024; Nievas Rosillo et al. 2025). The ability to efficiently perform statistical analyses and retrieve model parameters from state-of-the-art numerical simulations marks a paradigm shift in the study of blazars and other high-energy astrophysical sources. For instance, using this technique, we analyzed more than 700 SEDs of OJ 287 and investigated how spectral variations correlate with different sets of model parameters (Harutyunyan et al. 2025).

On the other hand, alongside the advancement of theoretical models, the quality of observational data is rapidly improving. The current volume of data already enables detailed multi-wavelength and multi-epoch analyses of blazar emission (e.g., Bégué et al. 2024; Nievas Rosillo et al. 2025; Harutyunyan et al. 2025). However, in many cases, contemporaneous coverage across the full electromagnetic spectrum is not available. This incomplete coverage introduces uncertainty regarding how reliably model parameters can be determined when some spectral bands are missing. This issue is critical, as these parameters directly inform our understanding of the physical conditions within blazar jets. Furthermore, the SEDs of LSP, ISP, and HSP blazars differ significantly. As a result, the absence of data in a given energy band does not impact all classes equally—certain bands are more informative for specific source types. Addressing this issue is the main objective of this paper. Using one representative blazar from each subclass (LSP, ISP, and HSP), we systematically investigate how the exclusion of data from specific bands affects the outcome of spectral fitting. This analysis allows to quantify the role of different energy bands in determining model parameters and provides guidance for evaluating the reliability of model outputs based on the available data coverage.

The current study is focused on the issue of missing bands in the spectral coverage of LSP, ISP, and HSP, which within each group share common spectral properties outside of flaring states. In principle, missing spectral bands can also affect population-level studies of LSP, ISP, and HSP but this is outside the scope of the present paper.

The paper is organized as follows. In Section 2, we introduce the three blazars selected for this study: OJ 287, TXS 0506+056, and Mrk 421. Section 3 describes the SSC model adopted for the analysis and presents the modeling results for each source. In Section 4, we explain the procedure used to generate synthetic datasets and how different combinations of spectral coverage are constructed to mimic various observational scenarios. Section 5 presents the main results of our parameter recovery analysis. The discussion and conclusions are provided in the Sections 6 and 7, respectively.

# 2. SOURCE SELECTION

The classification of blazars based on the location of the synchrotron peak—into LSPs, ISPs, and HSPs is not only a phenomenological distinction but also reflects fundamental differences in the underlying physical processes. Each subclass tends to show a typical range for both the synchrotron and inverse Compton peak frequencies and these characteristic spectral properties provide valuable insights into the physical conditions within the jet, such as the efficiency of particle acceleration, the energy distribution of emitting particles, the magnetic field strength, and the emission region size. Therefore, when modeling the SEDs of blazars belonging to different categories, it is crucial to identify which model parameters can be reliably constrained and which remain poorly determined. This depends largely on the availability and quality of observational data across specific energy bands. Since each blazar subclass tends to exhibit emission features in distinct parts of the electromagnetic spectrum, the absence of data in key bands can significantly affect the robustness of parameter estimation, particularly for those related to particle energy distributions and magnetic field strength.

To explore the impact of data availability and the consequences of missing observational coverage on the determination of model parameters, we selected representative blazars from each synchrotron peak category-LSPs, ISPs, and HSPs—and modeled their SEDs. While

individual sources may exhibit distinct emission properties, we note that, on average, their spectral characteristics follow the general trends associated with their respective classes. The use of representative sources from each category is justified as the aim of this study is not to determine the physical origin of the emission in each blazar subclass, but rather to investigate how the presence or absence of observational data in specific energy bands affects the ability to constrain key model parameters.

The Fourth Catalog of Active Galactic Nuclei detected by the Fermi-LAT (Data Release 3; Ajello et al. 2022) includes a total of 1,379 BL Lac-type blazars, among which 353 are classified as LSPs, 347 as ISPs, and 425 as HSPs. The remaining 254 sources lack a reliable classification. Among the LSPs, we selected OJ 287, a bright blazar located at a redshift of z = 0.307. Although OJ 287 exhibits a mixed behavior in the X-ray band—with the emission sometimes corresponding to the tail of the synchrotron component—we selected a period that clearly shows LSP characteristics. For the ISP category, we choose TXS 0506+056, at redshift z = 0.337, which was associated with a VHE neutrino detection during a flaring episode and has since been continuously monitored across multi-walength bands. We note that TXS 0506+056 has been classified as a "masquerading BL Lac". However, the optical spectrum of this source only shows extremely weak emission lines (Padovani et al. 2019), implying that any external photon field must be faint compared to the bright Doppler-boosted jet, and does not significantly affect the SED modeling. For the HSPs, we selected Mrk 421, at redshift z = 0.031, one of the most extensively studied blazars in the context of multi-wavelength observations. These three source were selected due to their extensive multiwavelength coverage. However, any other source from these categories with similarly strong data coverage could have been used. We note that a small redshift is an asset for the analysis. Indeed, considering sources at larger distances would result in larger uncertainties in the data used for the fit, and even possibly their non-availability.

The data for OJ 287 and TXS 0506+056 were obtained from the Markarian Multiwavelength Data Center<sup>6</sup> (MMDC; Sahakyan et al. 2024a), a novel database, developed in cooperation with the Firmamento platform<sup>7</sup> (Tripathi et al. 2024), that provides time-resolved SEDs of blazars. The multiwavelength light curves of both sources were examined to identify epochs with-

<sup>6</sup> http://mmdc.am

<sup>&</sup>lt;sup>7</sup> http://firmamento.nyuad.nyu.edu

out strong flaring activity in the optical/UV, X-ray, and  $\gamma$ -ray bands. While mild variability is always present, these epochs correspond to comparatively low-activity states, free of pronounced flux enhancements that could modify the emission level and spectral shape. Selecting such periods reduces the risk of biasing the modeling results due to transient flares. For Mrk 421, we used data from the multi-wavelength campaign in 2009, which provides extensive coverage across the electromagnetic spectrum (Abdo et al. 2011).

The broadband SEDs of OJ 287, TXS 0506+056, and Mrk 421 are shown in Figure 1. The gray points represent archival data extracted from MMDC/Firmamento databases, while the blue points correspond to the dataset selected for modeling in the present study. As illustrated, the selected data represent an average emission state for each source, reducing the influence of flaring episodes and providing a consistent picture of their emissions.

### 3. THE SSC MODEL

The SED of blazars typically exhibits two broad components. In the case of BL Lacs, they are conventionally explained using the SSC model (Ghisellini et al. 1985; Maraschi et al. 1992; Bloom & Marscher 1996) which is adopted in our study. Within this model, the lowerenergy peak is attributed to synchrotron radiation from relativistic electrons, whereas the HE peak arises from inverse Compton scattering of these synchrotron photons by the same electron population. In this work we restrict our analysis to BL Lac objects; FSRQs, which require external Compton components, are not considered. We employ a one-zone SSC scenario in which all radiation is produced within a single homogeneous emitting region. This contrasts with two-zone or multi-zone models, where spatially distinct regions—typically associated with separate acceleration and cooling zones—can each contribute to the observed broadband emission.

In this study, we analyze the broadband emission from BL Lac type blazars using an advanced modeling technique introduced by Bégué et al. (2024) which is available through the MMDC platform (Sahakyan et al. 2024a). Unlike traditional numerical computations, this method replaces computationally intensive numerical modeling with a convolutional neural network (CNN) trained on radiative outputs of physical simulations. The CNN acts as a surrogate for the traditional numerical solver: it reproduces the same radiative solutions, preserves the underlying physics of particle injection and cooling, and has been validated against a large grid of numerical models (Bégué et al. 2024). Thus, the method is fully consistent with standard SSC modeling,

differing only in computational efficiency. The methodology and model setup are described in detail in Bégué et al. (2024). The analogous external Compton modeling is described in Sahakyan et al. (2024b) and the lepto-hadronic model in Sahakyan et al. (2025). Below we briefly summarize the main assumptions of the model.

Within an SSC model, the emission is produced from a spherical emission region with radius R and filled with a tangled magnetic field of strength B. Electrons are injected into this region at a rate described by a power-law spectrum with an exponential cut-off:

$$\dot{Q} = Q_{e,0} \gamma^{-p} \exp\left(-\frac{\gamma}{\gamma_{\text{cut}}}\right) \tag{1}$$

where  $Q_{e,0}$  normalizes the injection rate, p is the powerlaw index,  $\gamma_{\min}$  is the minimum Lorentz factor of the injected electrons, and  $\gamma_{\text{cut}}$  is the maximum Lorentz factor. These electrons cool as they emit synchrotron emission and interact via these synchrotron photons by inverse Compton scattering. The region is assumed to move relativistically toward the observer with a Lorentz factor  $\Gamma$ , and the jet is viewed at an angle approximately  $1/\Gamma$ , leading to a Doppler amplification with a factor  $\delta \approx \Gamma$ .

The model depends on seven free parameters: the electron spectral index p, the minimum and maximum Lorentz factors of the injected electrons ( $\gamma_{\min}$  and  $\gamma_{\text{cut}}$ ), the magnetic field strength B, the size of the emitting region R, the Doppler factor  $\delta$ , and the electron luminosity  $L_{\text{e}}$ , which is defined as:

$$L_e = \pi R^2 \delta^2 m_e c^3 \int_1^\infty \gamma \, Q(\gamma) \, d\gamma. \tag{2}$$

where Q is such that  $\dot{Q} = Q/t_{\rm dyn}$ , with  $t_{\rm dyn} = R/c$ . Note that the density of emitting electrons can be retrieved from the electron luminosity, Doppler boost and radius of the emitting region. The number of free parameters can be reduced when variability time is known but we keep the discussion general and do not restrict the analyses to pre-defined variability time scale. Instead we test how the spectral information only can constrain the parameters.

During the modeling, the first step is to retrieve the model parameters by optimization through maximization of the Gaussian likelihood function. To explore the parameter space and obtain their posterior distributions, we employ the MultiNest algorithm (Feroz et al. 2009), a nested sampling technique suitable for efficient Bayesian inference in high-dimensional spaces. We use 1000 active points and set the sampling tolerance to 0.5 to ensure a balance between computational efficiency and convergence accuracy.

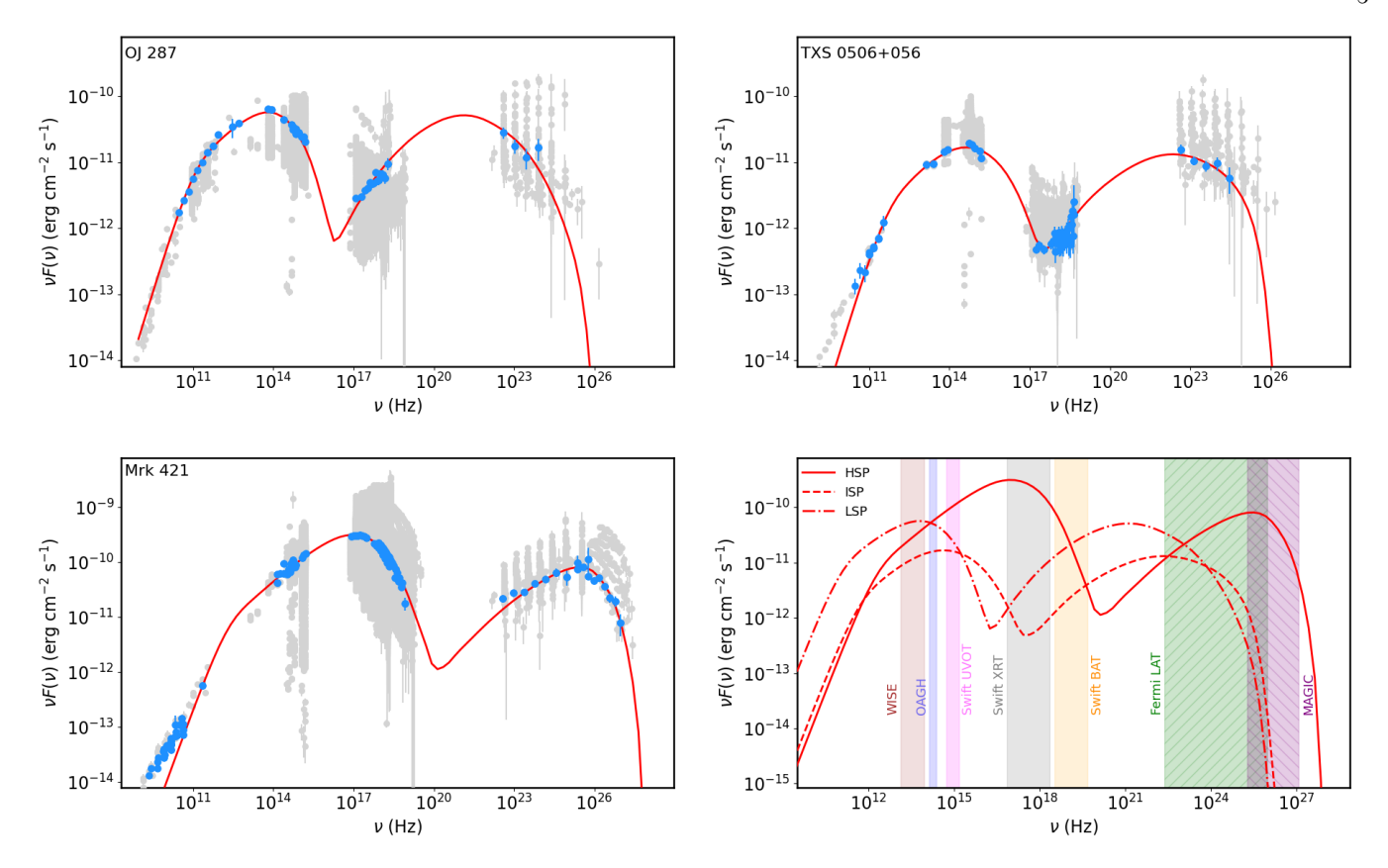


Figure 1. Observed SEDs of the three selected sources. Top left: the LSP blazar OJ 287. Top right: the ISP blazar TXS 0506+056. Bottom left: the HSP blazar Mrk 421. The data used for fitting are shown in blue, and the best-fit model is represented by the red line. Archival data retrieved from MMDC and Firmamento are shown in gray. Bottom right: best-fit models for all three blazars, displayed together with the instrumental bands used in this analysis. We note that the redshifts of these blazars differ, and therefore their observed fluxes also strongly differ. Studying the systematics induced by the different flux levels is beyond the scope of this work.

The results of the SED modeling are shown in Figure 1, with the model corresponding to the maximum likelihood (best-fit parameters) highlighted in red. The corresponding parameters are provided in Table 1. The SED of OJ 287, shown in the top left upper panel in Figure 1, is satisfactory modeled within the SSC model. The particle energy distribution is characterized by a spectral index of  $p = 2.18 \pm 0.2$ , and the electrons are accelerated up to a maximum Lorentz factor of  $\log_{10}(\gamma_{\rm cut}) = 3.98 \pm 0.3$ , with a minimum Lorentz factor of  $\log_{10}(\gamma_{\rm min}) = 2.37 \pm 0.3$ . The magnetic field in the emitting region is  $\log_{10}(B/G) = -1.71 \pm 0.2$ , while the Doppler factor  $\delta$  is estimated to be  $\delta$  =  $25.68\pm5.5$ . The radius of the emitting zone is inferred to be  $\log_{10}(R/\text{cm})=17.66\pm0.1$ . The electron luminosity,  $L_e=1.35\times10^{46}~\text{erg.s}^{-1}$  dominates over the magnetic luminosity  $L_{\rm B} = \pi c R^2 \delta^2 B^2 / 8\pi \approx 2 \times 10^{44} \text{ erg.s}^{-1}$ , so the jet is particle-dominated which is consistent with expectations for luminous BL Lac-type blazars.

In the case of TXS 0506+056 (upper right panel in Figure 1), the SSC modeling similarly provides an ad-

equate modeling of the selected SED. The electron distribution exhibits a spectral slope of  $p=2.20\pm0.2$  and a minimum and maximum Lorentz factor respectively of  $\log_{10}(\gamma_{\min})=2.39\pm0.3$  and  $\log_{10}(\gamma_{\rm cut})=4.53\pm0.2$ , indicative of highly energetic leptons within the jet. The magnetic field strength is relatively low, with  $\log_{10}(B/G)=-1.01\pm0.3$ , while the size of the emission region is estimated to be  $\log_{10}(R/{\rm cm})=16.98\pm0.3$ . The Doppler factor derived from the modeling is  $\delta=19.97\pm6.1$ . The inferred luminosities again show a particle-dominated jet composition.

For Mrk 421, shown in the lower panel in Figure 1, the observations reflects a typical HSP blazar with strong X-ray and TeV components. The electron spectrum has an index of  $p=2.15\pm0.1$ , with the maximum electron Lorentz factor reaching  $\log_{10}(\gamma_{\rm cut})=5.49\pm0.1$ . The SSC fit constrains the magnetic field to  $\log_{10}(B/{\rm G})=-1.32\pm0.2$ , and the minimum electron Lorentz factor is found to be  $\log_{10}(\gamma_{\rm min})=2.68\pm0.2$ . The emission region has a characteristic size of  $\log_{10}(R/{\rm cm})=16.44\pm0.3$ , moving with a Doppler factor of  $\delta=34.04\pm5.6$ .

The peak frequency of the synchrotron component is set by the relation between the magnetic field strength B and the maximum electron Lorentz factor  $\gamma_{\rm cut}$ :  $\nu_p \propto \gamma_{\rm cut}^2 B$ . From the results of our fits provided in Table 1, we find that B remains steady between  $10^{-2}$  and  $10^{-1}{\rm G}$  with rather large uncertainties, while  $\gamma_{\rm cut}$  increases from  $10^4$  to  $10^{5.5}$  from the LSP to the HSP. This seems to indicate that, at least for the sources considered here, the increase in observed frequency is primarily due to an increasing  $\gamma_{\rm cut}$ , indicating more favorable particle acceleration properties for HSPs. A firm statistical analysis of this interpretation is outside of the scope of the paper and will be investigated elsewhere.

#### 4. SYNTHETIC DATA GENERATION AND FIT

The modeling results shown in Figure 1, along with the corresponding parameters listed in Table 1, demonstrate that the different subclasses of blazars—LSP, ISP, and HSP—are characterized by distinct physical conditions and electron populations responsible for the emission. However, we do not perform a direct comparison of the physical parameters across different blazar types, as the goal of this work is not to interpret the intrinsic physical differences between these sources. Instead, our focus is on understanding how the availability or absence of observational data in specific energy bands influences the reliability of parameter estimation. The parameters listed in Table 1 are used as reference values, and for each blazar type, synthetic SEDs are generated and modeled using the same theoretical framework. A statistical analysis is then performed to evaluate which parameters can be reliably constrained and which remain poorly determined under different observational conditions.

In order to investigate the role of specific energy bands in parameter estimation, we selected the following instruments:

- Wide-field Infrared Survey Explorer (WISE) Infrared photometry data were used across four bands (3.4, 4.6, 12, and 22  $\mu$ m) (Wright et al. 2010).
- Observatorio Astrofísico Guillermo Haro (OAGH) Near-infrared observations in the H, J, K bands  $^8.$
- Ultraviolet/Optical Telescope (UVOT) onboard the Neil Gehrels Swift Observatory (hereafter Swift) - Ultraviolet measurements in UVW1,

- UVM2, and UVW2 filters, and optical measurements in the V, B, U bands (Roming et al. 2005).
- X-ray Telescope (XRT) onboard Swift X-ray observations in the 0.3–10 keV range (Burrows et al. 2005).
- Burst Alert Telescope (BAT) onboard Swift Hard X-ray observations covering the 14–195 keV range (Krimm et al. 2013).
- Large Area Telescope (LAT) onboard the Fermi Gamma-ray Space Telescope (Fermi-LAT)  $\gamma$ -ray data in the 0.1–400 GeV range (Atwood et al. 2009).
- Major Atmospheric Gamma Imaging Cherenkov Telescopes (MAGIC) - VHE γ-ray observations in the 0.08–5.0 TeV range (Aleksić et al. 2016).

These bands were chosen as they provide coverage across a broad range of wavelengths, as can be seen in the bottom right panel of Figure 1.

It is important to note that this study is not focused on the specific instruments listed above, but rather on the energy ranges they represent. Our aim is to assess the influence of data obtained in the infrared, optical, ultraviolet, X-ray, and  $\gamma$ -ray band on parameter estimation, independent of the specific characteristics of individual instruments. For instance, the conclusions drawn here would remain valid if data from other instruments operating in similar bands were used—such as replacing Swift-UVOT with any other ultraviolet or optical instrument, Swift-BAT with NuSTAR, or MAGIC with H.E.S.S., VERITAS or the upcoming Cherenkov Telescope Array Observatory (CTAO). We emphasize that our analysis is performed on already processed data in the  $\nu-\nu F_{\nu}$  representation. Therefore, instrumentspecific observational methods, calibration procedures, or raw data systematics are not taken into account in this analysis. If we performed the modeling on observed data (forward-folding), the choice of instrument and its technical characteristics would indeed play a critical role. This is an important aspect that should be tested in the future. By working with homogenized spectral data products, we ensure that our conclusions reflect the impact of spectral coverage rather than instrumentspecific effects.

The bottom right panel of Figure 1 shows the energy ranges covered by the selected instruments, overlaid with representative SED models for LSP, ISP, and HSP blazars, shown as dot-dashed, dashed, and solid lines, respectively. It is evident that the selected bands sample different regions of the SED depending on the blazar

<sup>8</sup> http://astro.inaoep.mx/en/observatories/oagh/

	OJ 287	TXS 0506+056	Mrk 421	
Parameters	LSP	ISP	HSP	
p	$2.18 \pm 0.2$	$2.20 \pm 0.2$	$2.15 \pm 0.1$	
$\log_{10}(\gamma_{ ext{cut}})$	$3.98 \pm 0.3$	$4.53 \pm 0.2$	$5.49 \pm 0.1$	
$\log_{10}(\gamma_{\min})$	$2.37 \pm 0.3$	$2.39 \pm 0.3$	$2.68 \pm 0.2$	
$\delta$	$25.68 \pm 5.5$	$19.97 \pm 6.1$	$34.04 \pm 5.6$	
$\log_{10}(B/[\mathrm{G}])$	$-1.71 \pm 0.2$	$-1.01 \pm 0.3$	$-1.32 \pm 0.2$	
$\log_{10}(R/[\mathrm{cm}])$	$17.66 \pm 0.1$	$16.98 \pm 0.3$	$16.44 \pm 0.3$	
$\log_{10}(L_0/[\text{erg s}^{-1}])$	$46.13 \pm 0.2$	$45.00 \pm 0.3$	$43.77 \pm 0.1$	

44.30

**Table 1.** Model parameters describing the three selected SEDs shown in Figure 1.

Table 2. Definitions of observation bands in each of the 21 cases used in the analysis performed in this paper.

44.11

42.88

Case	WISE	OAGH	Swift-UVOT	Swift-XRT	Swift-BAT	Fermi-LAT	MAGIC
1	No	No	No	Yes	No	Yes	Yes
2	No	No	Yes	No	No	Yes	Yes
3	No	No	Yes	Yes	No	No	Yes
4	No	No	Yes	Yes	No	Yes	No
5	Yes	No	No	Yes	No	Yes	Yes
6	Yes	No	Yes	No	No	Yes	Yes
7	Yes	No	Yes	Yes	No	No	Yes
8	Yes	No	Yes	Yes	No	Yes	No
9	No	No	Yes	Yes	No	Yes	Yes
10	No	No	Yes	Yes	Yes	Yes	No
11	No	Yes	Yes	Yes	No	Yes	No
12	Yes	No	Yes	Yes	Yes	Yes	No
13	Yes	Yes	Yes	Yes	No	Yes	No
14	No	No	Yes	Yes	Yes	Yes	Yes
15	No	Yes	Yes	Yes	No	Yes	Yes
16	No	Yes	Yes	Yes	Yes	Yes	No
17	Yes	Yes	Yes	Yes	No	Yes	Yes
18	Yes	Yes	Yes	Yes	Yes	Yes	No
19	Yes	No	Yes	Yes	Yes	Yes	Yes
20	No	Yes	Yes	Yes	Yes	Yes	Yes
21	Yes	Yes	Yes	Yes	Yes	Yes	Yes

type. For instance, infrared to optical/UV data trace the rising part of the synchrotron component in HSPs, while the same bands encompass the synchrotron peak for ISPs and the HE tail of the synchrotron component in LSPs. Similarly, X-ray observations probe the HE tail of the synchrotron emission in HSPs, the transition region between synchrotron and inverse Compton components in ISPs, and the rising segment of the inverse Compton component in LSPs. HE and VHE  $\gamma$ -ray data span the entire inverse Compton component in HSPs but only capture its high-energy tail in LSPs and the peak of HE component in ISPs. As a result, the inclusion or exclusion of data from specific bands affects

 $\log_{10}(L_{\rm B}/[{\rm erg \ s^{-1}}])$ 

the parameter estimation differently depending on the blazar subclass. This highlights the importance of spectral coverage tailored to the source type when modeling broadband emission.

### 4.1. Mock data generation

To assess the robustness of the modeling approach under varying observational constraints, we constructed a set of representative cases encompassing a broad range of multi-wavelength data availability. These cases, summarized in Table 2, were designed to simulate different levels of data coverage, from sparse to dense. In this analysis, we assume that all data are quasi-

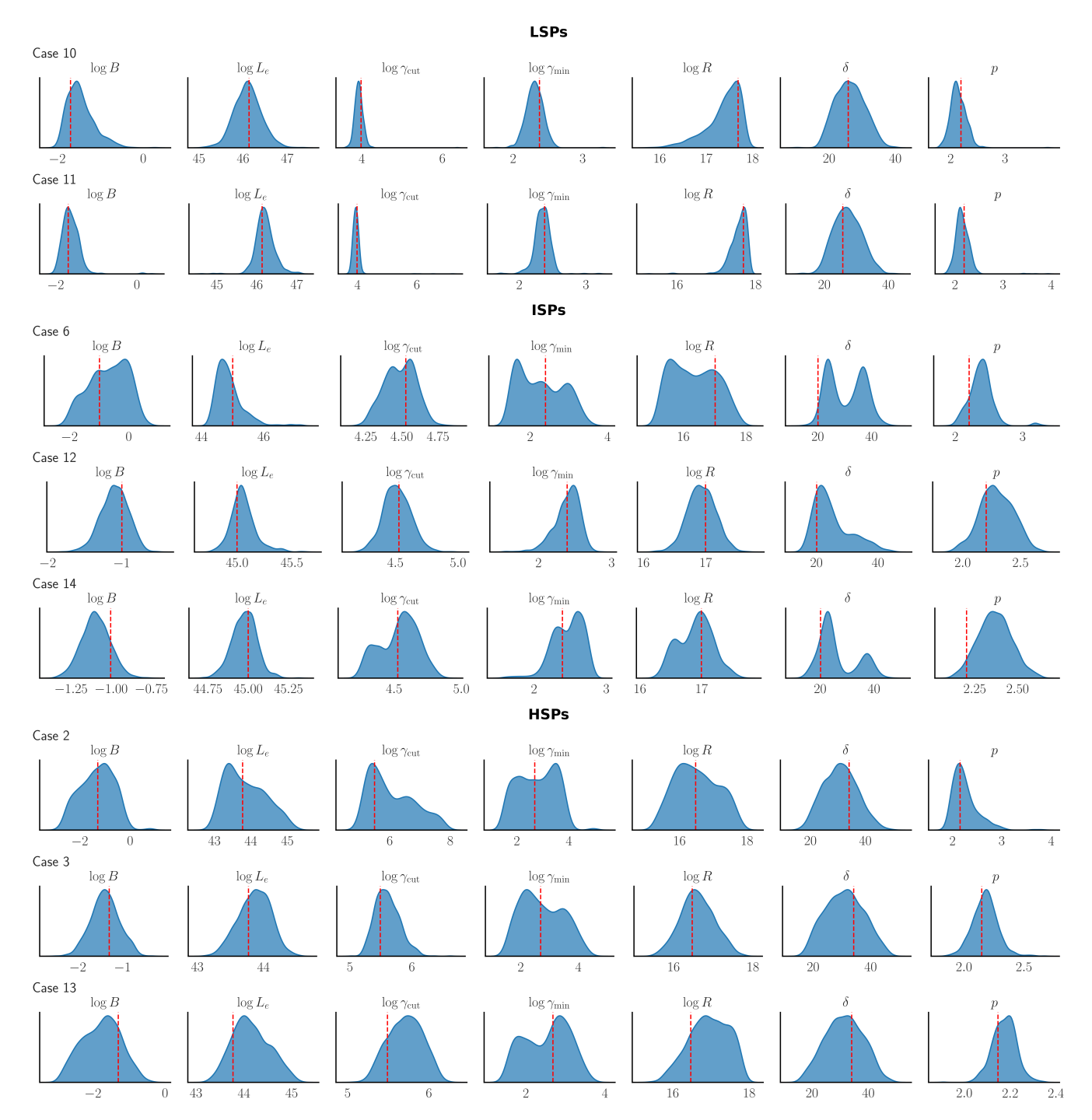


Figure 2. The density plots for selected LSP (top two rows), ISP (three middles rows), and HSP (three bottom rows) cases. The cases were chosen to show for each blazar type an acceptable recovery (HSP - case 3, ISP - case 12, LSP - case 11), a mediocre one (HSP - case 2, ISP - case 6) and an intermediate one (HSP - case 13, ISP - case 14, LSP - case 10) see the text for the details. The true parameter value, determined from the fits (see Table 1), is shown as the red dashed line. If the distribution is narrowly peaked around the red dashed line at its center, the corresponding parameter is likely adequately recovered. Note that this is in fact quantified by the coverage probability.

simultaneous, similarly to the assumption we made to analyze the three dataset in Section 2. In other words, spectral variation is not considered. At the low-coverage end, cases such as Case 1 and Case 2 include only a minimal subset of bands, combining, for example, X-ray and HE  $\gamma$ -ray observations (Swift-XRT, Fermi-LAT, and MAGIC), or ultraviolet and  $\gamma$ -ray data (Swift-UVOT, Fermi-LAT, and MAGIC), respectively. These

limited configurations are meant to reflect real-world scenarios where only partial simultaneous data are available. Intermediate coverage scenarios are represented by cases such as Case 10 and Case 14, which include contributions from most key instruments across infrared, optical, X-ray, and  $\gamma$ -ray bands, but may lack coverage in one or two specific domains (e.g., MAGIC or Swift-BAT). Finally, Case 21 provides an example of full multi-wavelength coverage, incorporating data from all considered instruments — WISE, OAGH, Swift-UVOT, Swift-XRT, Swift-BAT, Fermi-LAT, and MAGIC — allowing for the most comprehensive characterization of the source SED. This stratified sampling of data availability enables evaluation of the performance and reliability of the analysis framework under conditions ranging from highly constrained to optimally sampled observations. In principle, other configurations with available data can also be generated; however, we have selected scenarios ranging from minimal datasets to maximal coverage, that are most relevant (1) for the spectral analysis, and (2) with respect to available multiwavelength data.

For each configuration in Table 2 synthetic SEDs were generated to reflect the instrument-specific coverage. For each observational band, the synthetic flux values were derived by interpolating the underlying model SED (obtained from initial fit to the blazar data) at the logarithmic frequencies representative of the respective instruments. In the case of WISE, OAGH and UVOT the data were generated at exact frequencies covered by these instruments whereas five logarithmically spaced points were used within the BAT (14–195 keV), Fermi-LAT (0.1–400 GeV), and MAGIC (80–5000 GeV) bands. For the Swift-XRT band (0.3–10 keV), data were generated at logarithmically spaced frequencies with a step size of 0.1 in log-frequency space.

Uncertainties were implemented by adding Gaussian-distributed scatter to the interpolated flux values, with the standard deviation scaled to mimic realistic observational errors. In the X-ray and  $\gamma$ -ray domains, where background-dominated noise increases at higher energies, the fractional error was modeled as a linear function in log-frequency space, ranging from 5% at the lowest energies to 30% at the high end of each energy range. This energy-dependent uncertainty model was defined analytically for each instrument (e.g., Swift-XRT, Swift-BAT, Fermi-LAT, MAGIC) via a simple linear relation:

$$\sigma_{\log F} = a \cdot \log(\nu) + b,\tag{3}$$

with the slope a and intercept b computed to match the desired error scaling. In contrast, the optical and UV bands (OAGH and Swift-UVOT) were assigned a uni-

form uncertainty of 5%, reflecting their typically lower signal-to-noise ratios in standard exposures. This approach ensures that each synthetic dataset not only respects the spectral coverage of the selected instruments but also reflects realistic observational noise characteristics. Consequently, it enables a controlled yet physically grounded assessment of model performance across the full spectrum of data completeness.

## 4.2. Data fitting

For each case 1,000 synthetic SEDs were generated. The 21 cases of different band observations were then created from these 1000 SEDs, corresponding to a total of 21,000 realizations per blazar subclass (LSP, ISP, and HSP). This means that the same data realization is used in all cases, which only vary by which bands are being considered. The fitting procedure was executed on a local server utilizing a Docker-based implementation of the modeling code, publicly available through the MMDC platform<sup>9</sup>. The system was configured to process approximately 3,000 fits per hour, enabling completion of all 63,000 fits in less than 24 hours.

For illustration, we show on Figure 2 the kernel density estimations (KDE) of all recovered parameters for a selected few cases for each blazar type. The red dashed lines shows the true parameter values, determined from the fits (see Table 1). If it lies close to the maximum of the KDE, or at the center of the distribution, it is likely that the corresponding parameter is adequately recovered. Note that this is quantified by the coverage probability.

# 5. RESULTS

To assess the impact of spectral coverage on the reliability of model parameter recovery, we analyzed the fit results of the synthetic SEDs generated under various observational configurations. To quantify the accuracy of parameter estimation, we use the coverage probability, defined as the fraction of the 1000 synthetic fits whose  $1\sigma$  error intervals (i.e., fit value  $\pm \sigma_{\rm error}$ ) contain the true parameter value. The coverage property is a number between 0 and 1, where a value close to 1 (at least above the threshold of 0.68) represents a good coverage, meaning that most of the 1000 fits retrieved the expected values within  $1\sigma$ , while a value close to 0 means that none of the fit recovered the right parameter value within  $1\sigma$ , implying either a too constrained parameter value for which the error does not capture the generative value or an unreliable parameter estimation.

<sup>9</sup> www.mmdc.am

### 5.1. Low synchrotron peak: OJ287

For LSP sources, observations in the VHE  $\gamma$ -ray band are typically not available due to low flux levels, as the HE peak is in the MeV band. We therefore remove all cases considering the MAGIC band for this class of blazar, leaving a total of 9 configurations for the LSP scenario. The coverage probabilities for all model parameters across the remaining cases are summarized in Figure 3. Overall, the results indicate good coverage for almost all parameters, with values typically exceeding 0.9 for most parameters. Only the Doppler factor can be improperly retrieved, with a coverage probability dropping to  $\sim 0.8$  across cases. This is explained by the fact that all considered cases includes X-ray (Swift-XRT) and  $\gamma$ -ray (Fermi-LAT) data together with low energy data, which are critical for constraining the HE component of the SED which in turn determines parameters such as  $\log \gamma_{\rm cut}$ ,  $\log \gamma_{\rm min}$ , and p, as well as the normalization of the electron distribution. The latter, in combination with the magnetic field strength, is further constrained by lower-energy data.

It is interesting that the coverage for  $\log \gamma_{\rm cut}$  and p reaches or approaches unity across all cases, indicating a highly reliable recovery within  $1\sigma$  of these parameters under the SSC framework. In contrast, the Doppler factor  $\delta$  shows lower coverage values, ranging from 0.75 to 0.81, which shows a reduced sensitivity of this parameter to the available data. This suggests that, with the current observational data in the 9 cases,  $\delta$  remains poorly constrained for LSP sources. As an illustrative example, the density distributions for Cases 10 and 11 is shown in the upper panel of Figure 2. The red dashed lines shows the true parameter values, which lie near the centers of the corresponding density distributions in the most cases, confirming the high coverage levels.

### 5.2. Intermediate synchrotron peak: TXS 0506+056

For ISP sources, the synchrotron peak is observed at intermediate frequencies,  $10^{14} \rm Hz < \nu_{\rm syn} < 10^{15} \rm Hz$ , and the inverse Compton component can extend into the GeV–TeV band. Therefore, reliable parameter estimates for ISPs depend on capturing both the synchrotron and inverse Compton components with sufficient spectral coverage. In contrast to LSPs, the inclusion of VHE  $\gamma$ -ray-ray data is necessary for ISPs due to the higher flux levels expected in this band. Therefore, all 21 observational configurations were analyzed, and Figure 4 shows the resulting parameter coverage across all cases. The strongest constraints are found in Cases 8, 12, and 18, where five out of seven model parameters reach coverage above 0.9, as well as in Case 13, where four out of seven parameters exceed this thresh-

old. These cases include broad multi-wavelength coverage ranging from the infrared to TeV bands. Case 8 includes WISE, Swift-UVOT, SWIFT-XRT and Fermi-LAT. Case 12 includes WISE, Swift-UVOT, Swift-XRT, Swift-BAT and Fermi-LAT. Case 13 includes WISE, OAGH, Swift-UVOT, Swift-XRT, and Fermi-LAT data, while Case 17 includes a similar set with MAGIC data. This configuration enables strong constraints on the parameters  $\log \gamma_{\rm cut}$ ,  $\log \gamma_{\rm min}$ ,  $\log B$ ,  $\log L_e$  and  $\log R$ , as both the low- and high-energy slopes of the SED are well constrained. It is interesting that coverage for  $\log R$  and  $\log \gamma_{\min}$  also reach values above 0.9 in these cases, indicating that coverage across multiple energy bands can actually help to constrain geometrical and low-energy cutoff parameters. Relatively strong parameter recovery is also observed in Case 7, where all parameters exceed the 0.68 threshold, and  $\log B$  and  $\log L_e$  are constrained with coverage  $\geq 0.9$ .

Among all model parameters,  $\log L_e$  and  $\log \gamma_{\rm cut}$  are generally the best recovered, with coverage  $\geq 0.9$  in 14 and 10 cases, respectively. The parameter  $\log B$  also shows strong performance, exceeding 0.9 in five cases (Cases 7, 8, 12, 13, 18). In contrast, the Doppler factor  $\delta$  and the electron spectral index p are the most difficult parameters to recover, with minimum coverage values of 0.40 and 0.37, respectively. For example low coverage for p is observed in Case 19, alongside with Case 20 and 21. This is interesting as these three cases have the most comprehensive coverage of all our cases, only lacking a low-energy band for Case 19 and 20. For these three cases, the fitted values of the spectral index is found to be systematically larger than the generative one, while the error on this parameter is systematically small, resulting in a poor coverage probability. Since the data and their errors are generated independently for each instrument in our mock observation, this shows that each band is important and should be treated consistently to avoir systematic error in the fit.

Overall, the Doppler boost  $\delta$  is poorly constrained in the majority of cases, with only 6 out of 21 exceeding the 0.68 coverage threshold. This indicates that flux-based SED fitting alone is insufficient to robustly determine the Doppler factor and that additional information—such as variability timescales or source geometry—is required. The weakest overall parameter recovery is observed in case 6, where only two parameters achieve coverage above 0.68 and the others are below. Case 3 also performs relatively poorly, with no parameters reaching coverage above 0.9 and only three exceeding the 0.68 threshold.

Figure 2 (middle panel) presents the parameter distributions for Cases 6, 12, and 14. Case 12 demon-

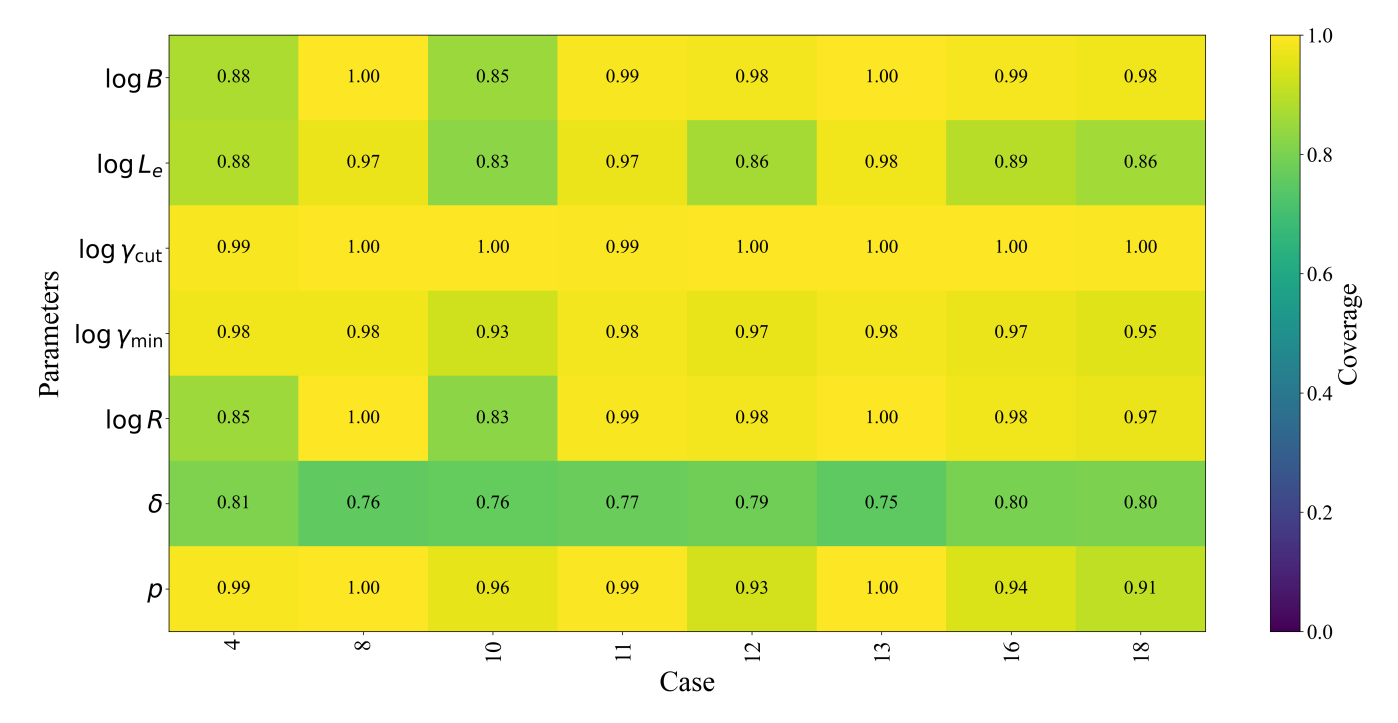


Figure 3. Density matrix for the LSP OJ 287 showing the coverage probability for each parameter (line) in each case (column). The number in each cell corresponds to the coverage probability, which is also encoded in the colormap. Yellow cells correspond to high coverage probability while green cells represent lower coverage probability. A high coverage probability means that the fit retrieve the true parameter within its uncertainty. For LSPs, only cases without MAGIC data are presented.

strates well-peaked density distributions for most parameters while Case 6 shows broad distributions, with only  $\log \gamma_{\rm cut}$  constrained. Case 14 represents an intermediate scenario: some parameters, such as  $\log L_e$  and  $\log B$ , are well constrained, while others remain weakly constrained due to gaps in observational coverage.

# 5.3. High synchrotron peak: Mrk 421

For HSP sources, the synchrotron peak typically lies in the UV or X-ray band, resulting in the HE component extending from a few GeV up to multi-TeV energies. Consequently, compared to LSP and ISP sources, observations in the X-ray and  $\gamma$ -ray bands, especially in the VHE  $\gamma$ -ray band, are essential for performing reliable SED modeling and parameter estimation. All 21 observational configurations were included in the analysis, allowing for a systematic assessment of the contribution of different data bases to the modeling and parameter recovery. Figure 5 presents the coverage probabilities for all model parameters across the 21 considered cases, and the KDE of a few selected cases (2, 3, 13) are shown in Figure 2.

The spectra of HSP sources have the broadest spectrum among the three source classes (LSP, ISP, HSP), leading to improved recovery of several model parameters. The electron spectral index p is the most reliably constrained parameter, with coverage exceeding 0.9 in

12 out of 21 cases. In particular, very high coverage (> 0.95) is achieved in Cases 3, 5, 7, 8 and 13. These cases consistently include one band at low, intermediate, and high energy. Since the rising slopes of both the synchrotron and inverse Compton components are sensitive to p, and since each of these components are covered by the set of instruments, a robust parameter estimation is possible. The cutoff energy  $\log \gamma_{\rm cut}$  is also well retrieved in seven cases (> 0.95), with coverage above 0.95 in Cases 3, 4, 7, 9, and 15. These configurations include Fermi-LAT and/or MAGIC data at high energy, as well as Swift-UVOT and Swift-XRT, allowing constraints on p and  $\log \gamma_{\rm cut}$  all-together. The LAT data primarily constrain p, while MAGIC or XRT data help determine the cutoff energy. Another parameter with high coverage (> 0.9) is the magnetic field strength log B, which is well constrained in Cases 3, 7, 9, 14, 15 and 20. These cases share a common observational setup, incorporating Swift-UVOT, Swift-XRT and Fermi-LAT data. This combination enables simultaneous constraints on both pand  $\log \gamma_{\rm cut}$  which, in turn, defines the synchrotron and inverse Compton peaks allowing to estimate  $\log B$ .

In contrast, parameters such as  $\log \gamma_{\min}$ ,  $\log R$ , and  $\delta$  are poorly constrained. For  $\log \gamma_{\min}$ , the coverage ranges from 0.53 to 0.69 in most cases, exceeding the 0.68 threshold only in Case 5. The Doppler factor  $\delta$  exhibits the lowest coverage among all parameters, being

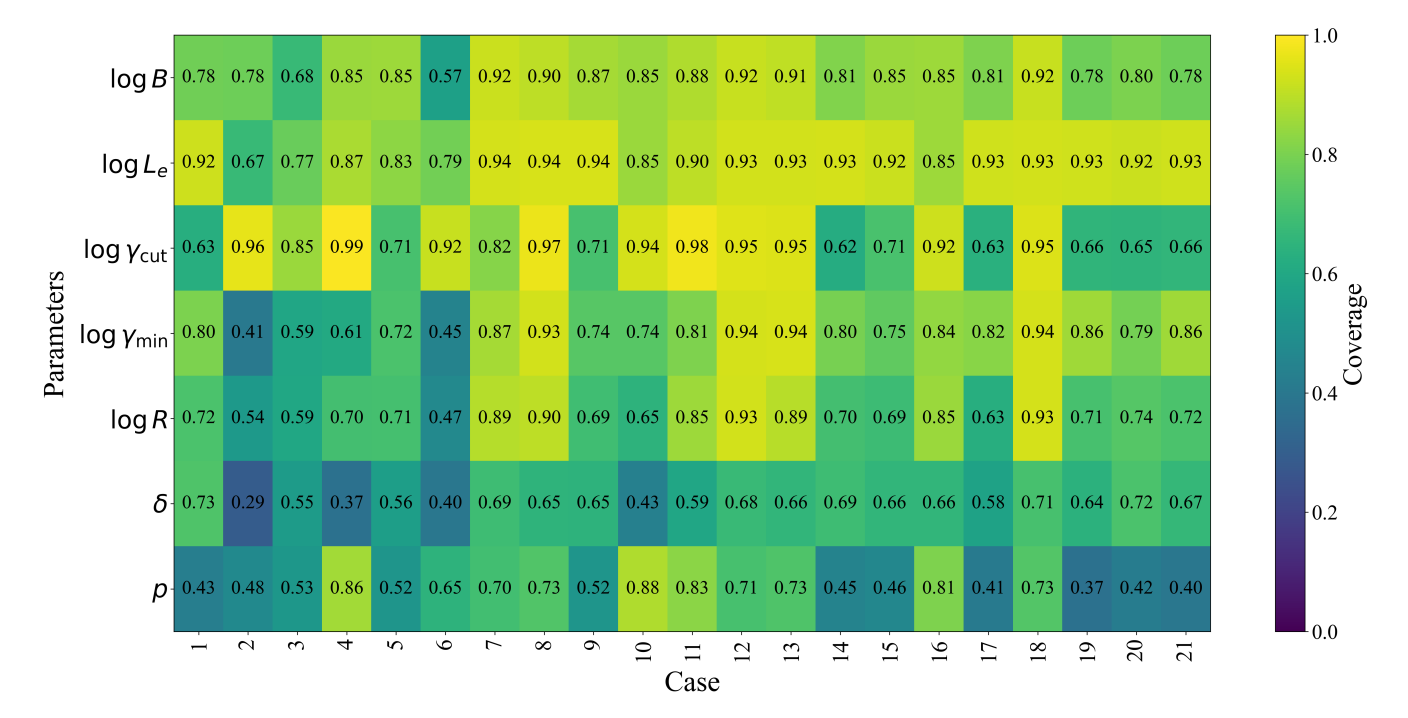


Figure 4. Same as Figure 3 but for the ISP TXS 0506+056.

below 0.65 in all cases. These results indicate that flux-based modeling is insufficient for reliably constraining the Doppler boost for an SSC model for HSPs. External constraint based on the variability time compared to the light crossing time would remove this parameter and maybe allow for better coverage of other parameters.

The cases with the highest number of parameters (5 out of 7 parameters) with coverage  $\geq 0.68$  are Cases 3, 7, 9, 14, 15, and 20. Cases 3, 9, and 15 show the strongest high-confidence estimates with 4 parameters with coverage  $\geq 0.90$ . Interestingly, in Case 3 where only Swift-UVOT, Swift-XRT, and MAGIC data are available p,  $\log \gamma_{\rm cut}$ ,  $\log L_e$  and  $\log B$  are confidently retrieved. In contrast, Cases 2 shows a poor coverage for most parameters and only p is recovered above the 0.68 threshold.

To illustrate representative cases, the distributions of the fitted parameters for Cases 2, 3, and 13 are shown in Figure 2 (three bottom panels). In Case 3, the distributions of the fitted parameters are narrow and centered around the true values (red dashed lines), consistent with the high coverage across nearly all parameters. Case 2, with limited multi-wavelength data, results in broader, less peaked distributions and reduced reliability for parameter estimates. Case 13 provides an intermediate scenario, where some parameters (e.g.,  $\log \gamma_{\rm cut}$ ) remain well constrained while others do not.

#### 6. DISCUSSION

Modeling the multiwavelength SEDs of blazars is one of the most effective approaches for understanding the physical properties of these sources, such as the particle energy distribution, magnetic field strength, Doppler boost and emission region size. However, the availability of observational data across the full electromagnetic spectrum is often incomplete, with some energy bands missing due to observational constraints or temporal gaps. Alternatively, understanding which minimal set of observation bands are required for reliably inferring the largest number of parameters is also important for multi-wavelength followup strategy. These raise an important question regarding which model parameters can still be reliably estimated when spectral coverage is incomplete. To address this, we selected three representative sources—one from each BL Lac blazar subclass (LSP, ISP, HSP)—and modeled their broadband emission within the SSC model. Based on the best-fit models, we generated synthetic SEDs by systematically simulating different observational configurations that reflect various degrees of spectral coverage. For each configuration, we produced 1,000 synthetic spectra for each of the 21 observation band configuration, yielding a total of 63,000 SEDs across the three source types. These datasets, corresponding to different wavelength availability, were fitted using a CNN surrogate model trained on radiative simulations, enabling efficient parameter estimation. Compared to the analysis presented in Apel et al. (2025), where the authors studied how different methods to perform the fit impact the values of the retrieved model parameters of an SSC model, here we systematically study how the presence and absence of each

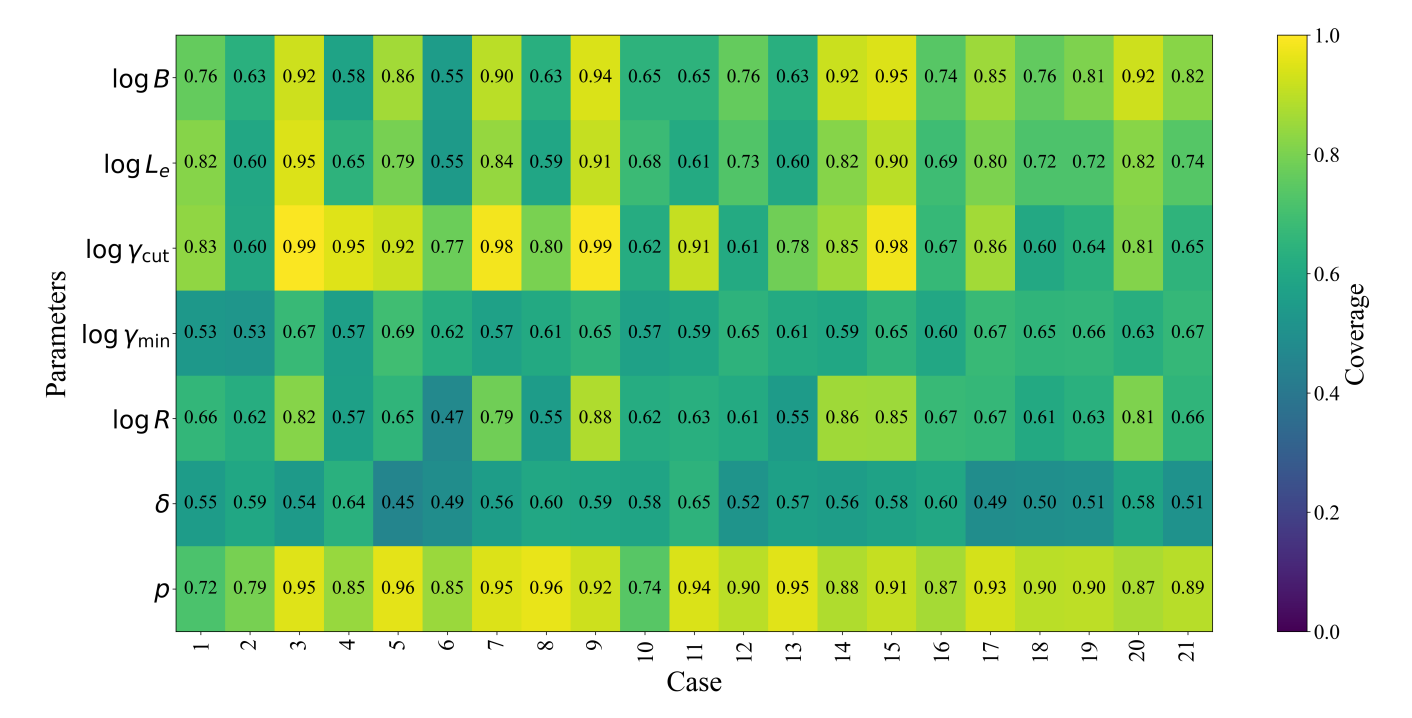


**Figure 5.** Same as for Figures 3 and 4, but for HSP.

observation band effect the reliability of parameter recovery.

The fit of the extensive synthetic dataset enables a systematic assessment of the robustness of parameter recovery based on observational coverage. Namely, this allows to quantify the role of individual spectral bands in constraining specific physical parameters. By analyzing the impact of data availability on the accuracy and reliability of recovering model parameters, it is possible to identify for each parameter which observational domains are critical for effective modeling and which ones contribute less significantly. In the following, we focus on ISP and HSP blazars, for which the interplay between synchrotron and inverse Compton components occurs across separated energy bands, making the identification of key constraints more nuanced. The LSP class is excluded from this discussion, as their SEDs show narrower separation between the synchrotron and inverse Compton peaks and any combination of optical/UV and X-ray with HE  $\gamma$ -ray data is generally sufficient to recover the model parameters.

### 6.1. Bands critical for ISP parameter estimation

The analysis of ISP blazars shows that reliable parameter recovery is achievable even in configurations with limited spectral coverage. For the cases with minimal data (Cases 1 to 4), which include only three observational bands, it is interesting that five out of the seven model parameters exceed the 0.68 coverage threshold for Cases 1 and 4. This demonstrates that, despite sig-

nificant gaps in spectral data, the majority of physical parameters can still be robustly estimated. In the intermediate cases with four-band coverage (Cases 5 to 8), parameter recovery improves further. Specifically, Case 7 yields reliable estimates for all parameters, with only the Doppler factor  $(\delta)$  and the spectral index p being characterized by a coverage factor smaller than 0.7.

As expected, configurations with broader spectral coverage tend to yield higher coverage values across multiple parameters. However, this does not imply that simply increasing the number of observed bands will always improve parameter recovery. In some cases, tighter constraints on one parameter can introduce degeneracies or limit the ability to constrain others, highlighting the complex interplay between model parameters. Based on Cases 1 and 4, the minimal set of energy bands required for effective modeling of ISP blazars includes:

- i) a combination of data in the X-ray, HE  $\gamma$ -ray, and VHE  $\gamma$ -ray bands, in which all parameters can be reliably recovered except for p and  $\log \gamma_{\rm cut}$ ; and
- ii) a combination of data in the optical/UV, X-ray, and HE  $\gamma$ -ray bands, in which all parameters are recoverable except for  $\delta$  and  $\log \gamma_{\min}$ .

The inclusion of these bands ensures coverage of both emission components and allows reliable inference of the underlying physical parameters.

### 6.2. Bands critical for HSP parameter estimation

Modeling the broadband SEDs of HSP blazars generally requires more stringent spectral coverage compared to ISPs. This is due to the fact that both the synchrotron and inverse Compton components peak at higher energies and parameter recovery becomes highly sensitive to the presence of data above the X-ray band. Among the configurations with minimal data coverage (i.e., 3-band observations; cases 1-4), only Case 3 yields reliable estimates (coverage > 0.68) for 5 out of 7 model parameters. Specifically, Case 3 includes Swift-UVOT, Swift-XRT and MAGIC. The combined data sets enable coverage of both the rising and falling segments of the synchrotron component or of the inverse Compton component in cases that include MAGIC data, thereby allowing a reliable recovery of the majority of the physical model parameters. The only parameters that are poorly recovered in this case are the Doppler factor  $(\delta)$ and the low-energy cutoff of the electron distribution  $(\log \gamma_{\min})$ . This suggests that even minimal configurations, if strategically composed, can capture the dominant SED features, and allow to confidently recover several model parameters.

Expanding the dataset to include four-band configurations (Cases 5-8), it is found that Cases 5 and 7 achieves accurate recovery of 5 parameters. Notably, Case 7 is identical to Case 3, but with the addition of WISE infrared data. However, the inclusion of IR data does not enhance the recovery of model parameters in this case, as both  $\delta$  and  $\log \gamma_{\min}$  remain poorly constrained. The lack of constraint on  $\log \gamma_{\min}$  arises from the fact that it sets a low-energy cutoff in the synchrotron spectrum that lies below the IR regime, thus falling outside the sensitivity range of the observed bands.

# 6.3. Importance of the results for CTAO

The upcoming CTAO promises to revolutionize our understanding of the HE universe in general, and blazars in particular (Cherenkov Telescope Array Consortium et al. 2019). The energy range of CTAO is comparable to that of MAGIC, though it extends to lower energies (from 20 GeV to 300 TeV) and provides higher sensitivity. Therefore, the results obtained in this work help identify which additional bands should be combined with CTAO observations to enable the most reliable parameter recovery. We consider six pairs of Cases—(10,14), (11,15), (12,19), (13,17), (16-20), and (18,21) —where, in each pair, one case includes MAGIC data and the other does not. The pairs differ in the additional observational bands included, allowing us to assess the impact of MAGIC data, and by extension CTAO data in various multi-wavelength configurations.

In the case of ISP blazars, the inclusion of VHE  $\gamma$ -ray data does not necessarily improve the recovery of model parameters and, in some configurations, systematically degrades it. This can be attributed to the spectral position of the VHE  $\gamma$ -ray band relative to the characteristic SED of ISPs. The inverse Compton component in these sources typically peaks at energies below the VHE  $\gamma$ ray range, meaning that observations in this band often probe only the steeply falling tail of the HE emission. As a result, data in this band provide limited constraining power on the peak location or spectral shape, and can even introduce biases when the fit attempts to reproduce fluxes that are not representative of the dominant emission regime. Moreover, when spectral coverage already includes data in the infrared, optical/UV, X-ray, and MeV/GeV  $\gamma$ -ray bands, the additional information from the VHE  $\gamma$ -ray band has marginal impact on the overall fit quality. This limitation does not apply in cases where MeV/GeV data are missing but there is good coverage in the other bands. For example, in Case 7, where Fermi-LAT data are absent, the inclusion of VHE  $\gamma$ ray observations led to the strongest parameter recovery. Therefore, for ISPs, the use of VHE  $\gamma$ -ray data (when MeV/GeV data are available) should be evaluated with care, as a well-balanced multi-wavelength configuration is often more effective for robust parameter estimation.

Conversely, in the case of HSP blazars (see Figure 5), the impact of MAGIC data is evident through consistent improvements across all pairs considered. For example, comparing Case 10 and Case 14, the addition of MAGIC data leads to improved estimates of  $\log B$ ,  $\log \gamma_{\rm cut}$ ,  $\log R$ , p and  $\log L_e$ . This indicates that MAGIC data help to better constrain the HE peak of the SED. A more complex example is the comparison between Case 11 and Case 15, where the inclusion of MAGIC is not required to recover  $\log \gamma_{\rm cut}$ , which already has a high coverage probability in Case 11. Interestingly, when broadband coverage is already extensive—as in Case 12 vs Case 19 and Case 18 vs 21—the impact of MAGIC is reduced. This suggests that low-energy data tightly constrain the synchrotron component and help define both ends of the electron energy distribution, making the additional information from MAGIC somewhat redundant in fully sampled SEDs. As in the ISP case, the Doppler factor  $\delta$  and injection Lorentz factor  $\log \gamma_{\min}$  remain poorly constrained regardless of the inclusion of MAGIC data.

In the modeling, it is important to discuss how individual data in the HE band contribute to constraining model parameters. We therefore examine whether the MAGIC band alone can provide sufficient constraints in the absence of *Fermi*-LAT data. To investigate this issue, we focus on two pairs of configurations: Cases 3

vs. 4 and Cases 7 vs. 8. In each pair, the only difference is the substitution of data from Fermi-LAT with MAGIC, allowing for a direct assessment of the constraining power of MAGIC data when Fermi-LAT data are unavailable. The pairs differ by the presence or absence of WISE infrared data, with Cases 3–4 excluding it and Cases 7–8 including it. For the ISP sources, the results indicate that replacing Fermi-LAT data with MAGIC data leads to a worse recovery of several key parameters. Specifically, comparing Cases 3 and 4, the spectral index p, magnetic field strength log B, and electron cutoff energy  $\log \gamma_{\rm cut}$  are better constrained in the Fermi-LAT data -only configuration. For instance, the recovery probability of p drops from 0.86 (case 4 with Fermi-LAT data) to 0.53 (case 3 with MAGIC data), with similar trends for  $\log B$  (from 0.85 to 0.68) and  $\log \gamma_{\rm cut}$  (from 0.99 to 0.85). Instead, when WISE data are included (Cases 7 vs. 8), the performance of including MAGIC data are equivalent to those of Fermi-LATIn this case, the low energy information provided by WISE help constraining the synchrotron component at low energy (e.g., see Giommi et al. 2024), and therefore improve the impact of MAGIC data in the recovery of the parameters. Only the recovery probability of  $\log \gamma_{\rm cut}$ worsen, from 0.97 to 0.82. This is because MAGIC data are at higher energy (from 80 GeV to 5 TeV) than Fermi-LAT (from 100 MeV to 400 GeV) and does not allow to capture the peak of the inverse Compton component. Clearly in this case, the improved sensitivity of CTAO at lower energy compared to that of MAGIC, will enable a better characterization of the inverse Compton scattering component and improve the parameter recovery performance.

For the HSP sources, the situation is reversed. Replacing Fermi-LAT data with MAGIC data results in systematically better recovery of key model parameters. When comparing Case 3 (MAGIC data-only) to Case 4 (Fermi-LAT data-only), we observe consistent improvements in coverage across nearly all parameters. Specifically, the recovery probability of the magnetic field strength  $\log B$  increases from 0.58 to 0.92, and the electron luminosity  $\log L_e$  also shows a notable improvement, from 0.65 to 0.95. A smaller improvement is also observed for  $\log R$  from 0.57 to 0.82. These differences highlight the critical role MAGIC observations plays in constraining both the synchrotron and inverse Compton peaks for HSPs. A similar trend is observed when WISE data are included (Cases 7 vs. 8): the addition of MAGIC data (Case 7) continues to yield better constraints than the Fermi-LAT data-only configuration (Case 8). For instance, the recovery probability of  $\log B$ improves from 0.63 and 0.9, and that of  $\log \gamma_{\rm cut}$  from 0.80 to 0.98. Overall, for HSP blazars, the presence of MAGIC data proves more effective than *Fermi*-LAT in enabling reliable parameter inference, likely due to the crucial spectral coverage of the inverse Compton peak provided by MAGIC for this blazar population.

These results indicate a clear divergence in the role of MAGIC observations for ISP and HSP blazars. For ISPs, MAGIC data alone cannot confidently constrain most SSC model parameters, unless additional constraints are available from the observations at lower energy bands. In contrast, for HSPs, MAGIC data leads to a systematic improvement in parameter recovery. This has important implications for future observations with CTAO. The extended sensitivity of CTAO at lower energies (compared to MAGIC), reaching down to tens of GeV and partially overlapping with the sensitivity window of Fermi-LAT, will be particularly important for ISP observations. It will enable robust parameter inference even when Fermi-LAT data are unavailable. For HSPs, CTAO is expected to provide comparable or improved performance relative to MAGIC, supporting accurate modeling of blazar high-energy emission.

# 7. CONCLUSIONS

In this work, we studied how the availability of multiwavelength observational data affects the reliability of parameter recovery within the SSC framework for three representative blazars: OJ 287 (LSP), TXS 0506+056 (ISP), and Mrk 421 (HSP). Using synthetic datasets generated under different spectral coverage scenarios, we quantified the degree to which physical model parameters can be recovered from flux-based SED fitting.

We have shown that for LSP blazars, a minimal combination of Swift-UVOT, -XRT, and Fermi-LAT data is sufficient to robustly constrain most SSC model parameters. For ISP blazars, a minimal set of observational bands capable of yielding reliable estimates for a significant number of parameters (5 out of 7) consists of either X-ray, HE  $\gamma$ -ray, and VHE  $\gamma$ -ray data, or optical/UV, X-ray, and HE  $\gamma$ -ray data. Similarly, for HSPs, the combination of optical/UV, X-ray, and VHE  $\gamma$ -ray data is sufficient to recover the majority of model parameters reliably. The contribution of VHE  $\gamma$ -ray data to parameter recovery differs between ISPs and HSPs. For ISPs, VHE  $\gamma$ -ray observations, when combined with lower-energy data (e.g., infrared), can effectively constrain model parameters even in the absence of HE  $\gamma$ -ray data. In contrast, for HSPs, VHE  $\gamma$ -ray data often encompass the peak of the high-energy component, leading to significant improvements in parameter recovery even when HE  $\gamma$ -ray data are unavailable.

To conclude, this study provides a practical road-map for the design of future multi-wavelength observation campaigns, identifying the minimal set of instruments needed to reliably constrain key physical parameters for each blazar subclass. It also serves as a diagnostic framework when modeling specific observational periods, allowing researchers to assess which parameters can be reliably inferred based on the available data.

#### ACKNOWLEDGMENTS

NS acknowledges the support by the Higher Education and Science Committee of the Republic of Armenia, in the frames of the research project No 23LCG-1C004.

#### REFERENCES

Abdo A. A., et al., 2010, ApJ, 716, 30 Abdo A. A., et al., 2011, ApJ, 736, 131 Abdollahi S., et al., 2022, ApJS, 260, 53 Ackermann M., et al., 2016, ApJL, 824, L20 Aharonian F., et al., 2007, ApJL, 664, L71 Ajello M., et al., 2022, ApJS, 263, 24 Aleksić J., et al., 2014, Science, 346, 1080 Aleksić J., et al., 2016, Astroparticle Physics, 72, 76 Ansoldi S., et al., 2018, ApJL, 863, L10 Apel F., Omeliukh A., Franckowiak A., Lederer J., 2025, arXiv e-prints, p. arXiv:2506.06080 Atwood W. B., et al., 2009, ApJ, 697, 1071 Bégué D., Sahakyan N., Dereli-Bégué H., Giommi P., Gasparyan S., Khachatryan M., Casotto A., Pe'er A., 2024, ApJ, 963, 71 Błażejowski M., Sikora M., Moderski R., Madejski G. M., 2000, ApJ, 545, 107 Bloom S. D., Marscher A. P., 1996, ApJ, 461, 657 Böttcher M., Reimer A., Sweeney K., Prakash A., 2013, ApJ, 768, 54 Burrows D. N., et al., 2005, SSRv, 120, 165 Cerruti M., Zech A., Boisson C., Emery G., Inoue S., Lenain J.-P., 2019, MNRAS, 483, L12 Cherenkov Telescope Array Consortium et al., 2019, Science with the Cherenkov Telescope Array, doi:10.1142/10986. Dermer C. D., Schlickeiser R., 1994, ApJS, 90, 945 Dermer C. D., Schlickeiser R., Mastichiadis A., 1992, A&A, 256, L27 Feroz F., Hobson M. P., Bridges M., 2009, MNRAS, 398, 1601 Finke J. D., Dermer C. D., Böttcher M., 2008, ApJ, 686, Gao S., Fedynitch A., Winter W., Pohl M., 2019, Nature Astronomy, 3, 88

Gasparyan S., Bégué D., Sahakyan N., 2022, MNRAS, 509,

Ghisellini G., Maraschi L., Treves A., 1985, A&A, 146, 204

2102

```
Giommi P., Sahakyan N., Israyelyan D., Manvelyan M.,
 2024, ApJ, 963, 48
Harutyunyan G., Sahakyan N., Bégué D., 2025, MNRAS,
 540, 582
IceCube Collaboration et al., 2018a, Science, 361, 147
IceCube Collaboration et al., 2018b, Science, 361, eaat1378
Keivani A., et al., 2018, ApJ, 864, 84
Krimm H. A., et al., 2013, ApJS, 209, 14
Mannheim K., 1993, A&A, 269, 67
Mannheim K., Biermann P. L., 1989, A&A, 221, 211
Maraschi L., Ghisellini G., Celotti A., 1992, ApJL, 397, L5
Mücke A., Protheroe R. J., 2001, Astroparticle Physics, 15,
  121
Mücke A., Protheroe R. J., Engel R., Rachen J. P., Stanev
 T., 2003, Astroparticle Physics, 18, 593
Murase K., Oikonomou F., Petropoulou M., 2018, ApJ,
  865, 124
Nievas Rosillo M., Acero F., Otero-Santos J., Vazquez
 Acosta M., Terrier R., Morcuende D., Arbet-Engels A.,
 2025, A&A, 693, A287
Padovani P., Giommi P., 1995, ApJ, 444, 567
Padovani P., et al., 2017, A&A Rv, 25, 2
Padovani P., Giommi P., Resconi E., Glauch T., Arsioli B.,
 Sahakyan N., Huber M., 2018, MNRAS, 480, 192
Padovani P., Oikonomou F., Petropoulou M., Giommi P.,
 Resconi E., 2019, MNRAS, 484, L104
Righi C., Tavecchio F., Pacciani L., 2019, MNRAS, 484,
Rodrigues X., Paliya V. S., Garrappa S., Omeliukh A.,
 Franckowiak A., Winter W., 2024, A&A, 681, A119
Roming P. W. A., et al., 2005, SSRv, 120, 95
Sahakyan N., 2018, ApJ, 866, 109
Sahakyan N., 2019, A&A, 622, A144
Sahakyan N., Giommi P., Padovani P., Petropoulou M.,
 Bégué D., Boccardi B., Gasparyan S., 2023, MNRAS,
 519, 1396
Sahakyan N., et al., 2024a, AJ, 168, 289
```

Sahakyan N., et al., 2024b, ApJ, 971, 70

Sahakyan N., Bégué D., Casotto A., Dereli-Bégué H., Vardanyan V., Khachatryan M., Giommi P., Pe'er A., 2025, ApJ, 990, 222

Sciaccaluga A., Tavecchio F., Landoni M., Costa A., 2024, A&A, 687, A247

Shukla A., et al., 2018, ApJL, 854, L26

Sikora M., Begelman M. C., Rees M. J., 1994, ApJ, 421, 153
Tripathi D., et al., 2024, AJ, 167, 116
Tzavellas A., Vasilopoulos G., Petropoulou M., Mastichiadis
A., Stathopoulos S. I., 2024, A&A, 683, A185
Urry C. M., Padovani P., 1995, PASP, 107, 803
Wright E. L., et al., 2010, AJ, 140, 1868